Nanograined Half-Heusler Semiconductors as Advanced Thermoelectrics: An Ab Initio High-Throughput Statistical Study

Jesús Carrete, Natalio Mingo, Shidong Wang, and Stefano Curtarolo**

Nanostructuring has spurred a revival in the field of direct thermoelectric energy conversion. Nanograined materials can now be synthesized with higher figures of merit (*ZT*) than the bulk counterparts. This leads to increased conversion efficiencies. Despite considerable effort in optimizing the known and discovering the unknown, technology still relies upon a few limited solutions. Here ab initio modeling of *ZT* is performed for 75 nanograined compounds—the result of accurate distillation with electronic and thermodynamic filtering techniques from the 79 057 half-Heusler entries available in the AFLOWLIB.org repository. For many of the compounds, the *ZT*s are markedly above those attainable with nanograined IV and III-V semiconductors. About 15% of them may even outperform *ZT* ≈ 2 at high temperatures. This analysis elucidates the origin of the advantageous thermoelectric properties found within this broad material class. Machine learning techniques are used to unveil simple rules determining if a nanograined half-Heusler compound is likely to be a good thermoelectric given its chemical composition.

1. Introduction

Harnessing the thermoelectric effect to scavenge electric power from waste heat has long been an attractive route in the pursuit of sustainable energy generation.[1] Despite recent progress, the goal of producing efficient thermoelectric materials remains elusive due to several challenging factors.[1,2] Effective thermoelectrics must have a high thermoelectric figure of merit:[3,4]

$$ZT = \frac{\sigma S^2 T}{\kappa} \tag{1}$$

where T, σ, S, and κ are temperature, the material's electrical conductivity, Seebeck coefficient, and thermal conductivity, respectively. κ, in turn, can typically be split into a sum of vibrational (κ_i) and electronic (κ_e) contributions. To design useful thermoelectric materials, the power factor ($P = \sigma S^2$) must be improved and the thermal conductivity reduced.

Nanostructuring approaches may significantly improve *ZT*.[5] Still, significant practical roadblocks remain to their production. Low-dimensional nanostructure (e.g., nanowires, thin films) methods can only be used in mesoscopic and macroscopic devices, and only after an assembly process demanding additional engineering and/or packaging.[6] Embedding nanophases to enhance bulk thermoelectric properties poses challenges due to controlling the size and morphology of precipitates.[7] A third alternative is the use of ad hoc nanocrystalline bulk materials having nanoscale grains,[8,9] core–shell structures,[10] or that undergo spinodal decomposition.[11,12] Such intrinsic features might ease synthesis.

Due to the high cost of experiments, studies of nanostructured materials for thermoelectric applications tend to focus on known compounds whose bulk properties are already promising. Well-known examples are Bi_2Te_3 and PbTe.[13,14] Alternatively, some researchers choose inexpensive and widely available materials, such as Si, and try to optimize their performance.[15] Very few studies, if any, have attempted to examine radically new materials from scratch.[16]

This work presents the first fully ab initio exploration of *ZT* for a large library of materials in a nanostructured configuration. We focus on half-Heusler (HH) compounds due to their typically high bulk power factors,[3] and the fact that many possible compositions are still unexplored. HH compounds are ternary XAB solids. Their crystalline structure consists of three inter-penetrated fcc lattices. **Figure 1** depicts the conventional and primitive cells of such structures.[2]

HHs are Heusler systems with a vacancy in one of the two doubly degenerate sublattices. This advantageous vacancy allows HHs to be easily doped, and their properties manipulated. Solubility limitations from size/electronegativity/character seen in other crystallographic prototypes are avoided.[17] Extensive studies on bulk forms or with nanoinclusions have been performed on a tiny number of HH alloys[18–20] (e.g., $NiSn_xBi_{1-x}Zr_yHf_{1-y}$[21] and $CoSn_xSb_{1-x}Zr_yHf_{1-y}$[22]).

Dr. J. Carrete, Dr. N. Mingo
CEA-Grenoble
17 Rue des Martyrs, Grenoble 38000, France
E-mail: natalio.mingo@cea.fr
Dr. S. Wang, Prof. S. Curtarolo
Center for Materials Genomics
Materials Science, Electrical Engineering
Physics and Chemistry
Duke University
Durham, North Carolina 27708, USA
E-mail: stefano@duke.edu

DOI: 10.1002/adfm.201401201

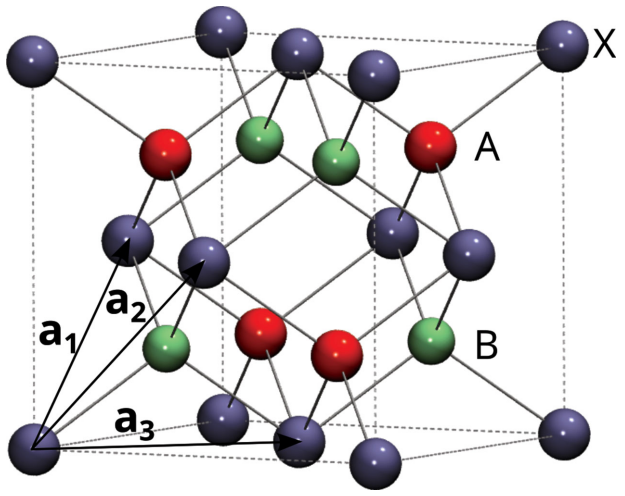

Figure 1. The cubic conventional cell of the half-Heusler structure (cF12). The three primitive vectors, $\{\mathbf{a}_1, \mathbf{a}_2, \mathbf{a}_3\}$, identify the standard primitive cell.[33]

Theoretical calculations have yet to characterize these compounds to their fullest extent.[23,24] Neighboring fields of research (e.g., spintronics, magnetism, topological insulators) are actively investigating Heusler systems via experimental and high-throughput approaches.[2,25,26]

We start by considering the 79 057 HH compounds included in the AFLOWLIB.org consortium repository.[27,28] This list contains all conceivable unique half-Heusler structures that can be built using elements from the list {Ag, Al, As, Au, B, Ba, Be, Bi, Br, Ca, Cd, Cl, Co, Cr, Cu, Fe, Ga, Ge, Hf, Hg, In, Ir, K, La, Li, Mg, Mn, Mo, Na, Nb, Ni, Os, P, Pb, Pd, Pt, Re, Rh, Ru, Sb, Sc, Se, Si, Sn, Sr, Ta, Tc, Te, Ti, Tl, V, W, Y, Zn, and Zr}. From this set, only compounds whose formation enthalpies are negative and optimal with respect to the elements' permutations are kept. We then discard any metallic compounds.

Supercell calculations are run to obtain full phonon dispersion relations of the remaining half-Heuslers. Only 450 compounds with fully real dispersions over the whole Brillouin zone (BZ) are kept. Mechanically unstable configurations are thus neglected.

Finally, the ternary phase diagrams for each of the 450 mechanically stable HHs are obtained from AFLOWLIB.org to assess their thermodynamical stability. More than 110 000 elemental, binary, and ternary phases are taken into account in these diagrams. Included are all relevant binary and ternary phases from the Inorganic Crystal Structure Database (ICSD).[29,30] Only the 77 thermodynamically stable HHs remain after these selection criteria are applied. Spin-polarized calculations reveal that two of the 77 have semimetallic ground states. Only the remaining 75 are chosen for further study. Note that checking our results against all the possible competing ground states from the ICSD database does not prevent other non-HH phases to appear at higher temperature, through vibrational-, magnetic-, or configurational-entropic stabilization (e.g., $NiMn_{1-t}Ti_tGe$).[31] The ICSD may also contain inaccuracies and is not guaranteed to be comprehensive. Ground states not listed in the ICSD can be found by global optimization methods poorly suited for high-throughput applications. However, in some cases our calculations predict the half-Heusler to be more stable than the non-HH isostoichometric phase reported in the ICSD. Specifically, this happens for CoAsHf, CoGeNb, CoGeTa, CoGeV, CoNbSi, CoSiTa, FeAsNb, FeAsTa, IrGeNb, NiGeHf, NiGeTi, NiGeZr, PdGeZr, PtGeZr, PtLaSb, RhAsTi and ZnLiSb. The ternary phase diagram of each of the 75 ternary compounds studied here can be found in the supplemental material of a previous study.[32]

The high density of grain boundaries in nanograined materials has a strong influence in the physics of thermal transport therein. Phonon and electron scattering at grain boundaries adds a contribution to the scattering probability density. This contribution is inversely proportional to the characteristic grain size.[34–36] In the nanograined limit, this contribution dominates over the factors that typically determine thermal conductivity in bulk semiconductors and alloys: three-phonon processes,[37] isotopic disorder,[38] alloying and embedded particles.[39] All mean free paths can be approximated by a single value λ, which is the same order of magnitude as the grain size. The general expressions for the phenomenological transport coefficients[40] can then be reduced to an approximate simplified form (see Experimental Section). This allows σ, κ_e and κ_i to become proportional to λ, while S remains independent. After manipulation of Equation 1, ZT reduces to a form independent from λ.

Hence, full knowledge of electronic and vibrational band structures for each compound becomes the essential ingredient for computing ZT. This approach needs no further approximations.

The results are expected to be robust compared to transport calculations in other regimes. An important issue is whether the nanograined limit can be achieved with realistic grain sizes. We estimate λ by comparing our calculated coefficients with the bulk values. For electrons, even in alloys, published mobilities are linked to mean free paths in the 10–100 nm range. For phonons, we calculate the bulk thermal conductivity of several tens of HHs using the Boltzmann transport equation. We find that typically $\lambda \gtrsim 10$ nm[32] at room temperature, and that it only decreases slightly at high temperatures. Thus, in parallel to what has been proven for Si,[8] the small-grain-size limit can be experimentally approached with nanograined HHs. This may allow for the development of high-performance thermoelectrics.

This approach to the nanograined-limit is a convenient simplification. A realistic description of grain boundaries would have to take into account the geometrical, chemical and electrical structures of those interfaces, which can give rise to energy- and charge-dependent scattering.[41,42] Those effects are likely to depend on the sample preparation procedure. On the other hand, having a simple descriptor like the nanograined-limit ZT is optimal for comparing compounds from a high-throughput perspective with respect to a single factor—nanograining. The use of a constant mean free path to describe boundary scattering has a long tradition;[43] more recent, finer studies support the idea that a best-fit constant mean free path can be found, although is likely to underestimate the experimental grain size.[41]

2. Results and Discussion

The temperature distributions of nanograined ZTs are presented in **Figure 2**, for both the n-type (top panel) and p-type

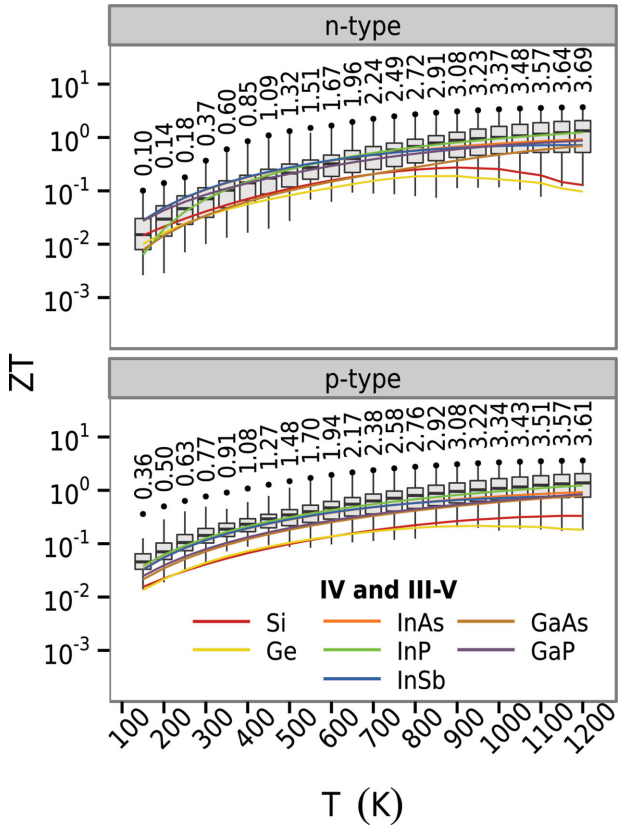

Figure 2. Distributions of nanograined *ZT* values for the HH compounds, at different temperatures. Boxes extend from the first to the third quartile, the median is represented by a horizontal black segment and whiskers have a length equal to 1.5 times the interquartile range. The maximum *ZT* at each temperature is drawn as a circle and its value annotated on the plot. Data for some elemental group-IV and binary III-V semiconductors are plotted for reference.

(bottom panel) doping regimes. The maximum carrier concentration allowed in the calculation is 10^{21} cm^{-3} to remain within the doping limits typical of experimental HH thermoelectrics[1] (Experimental Section). Detailed values for all compounds are included in the Supporting Information. For comparison, we also perform calculations for Si, Ge, and five common III–V binary semiconductors: InAs, InP, InSb, GaAs, and GaP; their results are superimposed in both panels. An experimental study[8] on the properties of nanostructured bulk Si reports values compatible with our estimation: for instance, at 500 K the reported *ZT* varies between 0.065 and 0.087 depending on milling conditions, which corroborates our 0.075 result.

The best considered elemental and binary thermoelectric semiconductors are InP and InSb, yet their corresponding curves in Figure 2 are usually around the median and never surpass the third quartile of the HH distribution. This indicates that most of the HHs outperform them at any given temperature. Indeed, many HH improve on InP by a very significant margin. The highest values of *ZT* are competitive with or better than the best reported for nanostructured bulk systems.[5] Especially remarkable are the values in excess of 2 achieved for $T > 600$ K.

Comparison of the panels in Figure 2 reveals that a typical (i.e., close to the median) p-type-doped HH is, at all but the highest temperatures, a much better thermoelectric than a typical n-type-doped HH. In contrast, the best n-type doped compounds are comparable with the best among the p-type-doped. Notably, the fraction of compounds achieving optimal thermoelectric efficiencies occurs when n-doped increases monotonically with temperature. This ranges from just 13% at 300 K, to 20% at 1000 K.

Qualitatively, these phenomena can be explained using a two-parabolic-band model. According to our band structure calculations, for 65% of compounds the effective mass of holes (m_h^*) is higher than that of electrons (m_e^*). This implies a generally higher optimized power factor for the p-type.[36] This explains the general trend of the medians, and allows enough exceptions to account for the maximum values.

Here we choose the best possible doping and try to reveal the factors contributing to improved performance. The power factor is key for selecting out these HHs from all other semiconductors considered, as shown in **Figure 3**a,b. While the thermal conductivities of the nanograined IV and III–V compounds are comparable to the HHs, their power factors barely reach the tenth percentile (most likely due to the fact that effective masses can be much higher in HHs).

We choose 300 K and 1000 K as representative of room- and high-temperature behaviors. We untangle some of the factors that determine desirable HH thermoelectrics. For this we use the Spearman rank correlation coefficient, Σ, which serves as an indicator of monotonic relationships between variables. We compute Σ among all the thermoelectric coefficients entering Equation 1. We also compute Σ between them and a data set of compound descriptors. These descriptors include the bandgap ε_g, the lattice parameter a_0 and the aforementioned effective masses.

We find that at 300 K, *ZT* and κ_e have a Σ value of –0.08. This becomes –0.35 at 1000 K. The increase in absolute value arises from the bigger role of heat transfer by charge carriers at high temperatures. The median contribution of charge carriers to κ increases from 5% at 300 K to 33% at 1000 K. Unsurprisingly, P/λ is a better predictor of *ZT* than κ/λ. This is due to its wider range of values ($\Sigma_{300\,K} = 0.86$ and $\Sigma_{1000\,K} = 0.89$ between P/λ and ZT; versus $\Sigma_{300\,K} = -0.25$ and $\Sigma_{1000\,K} = -0.44$ between κ/λ and ZT).

At both temperatures, the variation of the lattice contribution to κ over the set of compounds may be explained by the monotonically decreasing dependence of κ_l on a_0 ($\Sigma_{300\,K} = -0.79$ and $\Sigma_{1000\,K} = -0.81$). This is understandable taking the equipartition theorem into account, and considering the similitude of the expression for κ_l in Equation 5 with that of the vibrational specific heat. Likewise, the power factor exhibits a similar behavior at both room and high temperatures: P/λ depends most markedly on m_h^* ($\Sigma_{300\,K} = 0.85$ and $\Sigma_{1000\,K} = 0.79$) and on ε_g ($\Sigma_{300\,K} = \Sigma_{1000\,K} = 0.70$). This reflects the advantage of maximizing the contribution of majority carriers while keeping the minority carriers as unexcited as possible.

3.1. Simple Recipes for HH Thermoelectrics

Simple recipes are key factors for the transfer of theoretical results into practical technology. Rather than relying on

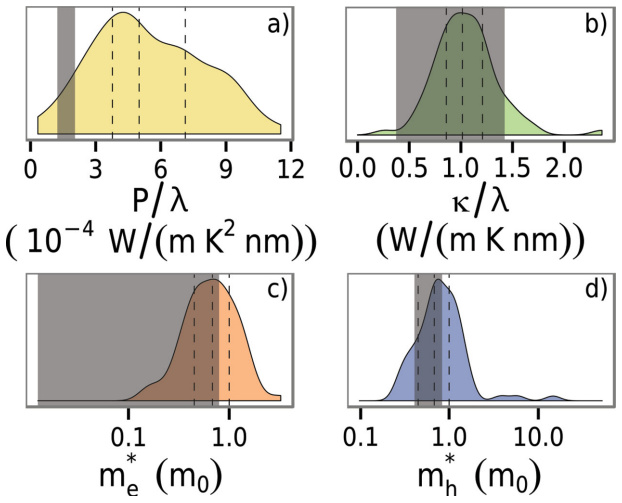

Figure 3. Frequency distributions among the 75 HHs of: a) power factors divided by grain size at 300 K, b) total thermal conductivities divided by grain size at 300 K, c) effective masses of electrons and d) effective masses of holes. Dashed vertical lines show the positions of the quartiles. The shaded areas span the values of each variable among the other seven semiconductors listed in Figure 2.

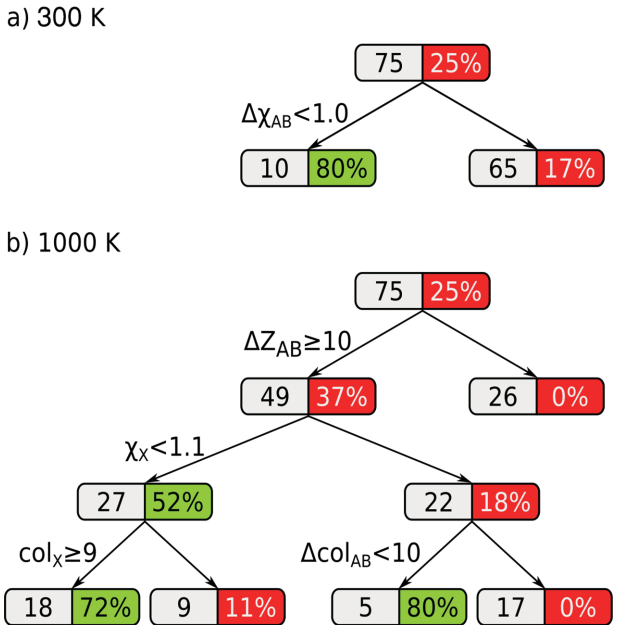

Figure 4. Classification trees for HH compounds at 300 K (top) and 1000 K. Printed on each node are the number of compounds it contains, and the fraction of them above the third quartile of the *ZT* distribution. Left-leaning branches correspond to increased percentages of compounds in the best-*ZT* category.

intuition, we opt for the use of machine learning techniques. These objective methods are capable of discovering potentially hidden rules.

First, we define the best thermoelectrics at a given temperature as those whose *ZT* is beyond the third quartile of the distribution. These are either $ZT > 0.20$ at 300 K, or $ZT > 1.66$ at 1000 K. Second, we then consider a few elements' properties $\{\psi^i\}$: atomic numbers (*Z*) and masses, positions in the periodic table (column/row, col/row), atomic radii (*r*), Pauling electronegativities[44] and Pettifor's chemical scales (χ).[45] Third, from each property ψ we build three descriptors: the property value for element *X*, ψ^i_X; the averaged property for elements A, B, $\bar{\psi}^i_{AB} = \frac{\psi^i_A + \psi^i_B}{2}$ (preserving choice A ↔ B); and the absolute property difference for elements A, B, $\Delta\psi^i_{AB} = |\psi^i_A - \psi^i_B|$. Fourth, we grow a decision tree classifying the compounds in the best-*ZT* category by performing a binary split of the data minimizing the Gini impurity increase.[46] As a stop-branching criterion, no further splits are attempted within nodes with less than 15 compounds. Finally, the fully grown tree is pruned back to the point where the cross-validation error is minimized. The procedure converges to the trees shown in **Figure 4**. The room- and high-temperature trees put 83% and 89% of the compounds in the correct group, respectively.

The key variable in each classification is the one at the top of each tree. Although high thermoelectric efficiencies at room and at high temperature are highly correlated ($\Sigma = 0.82$ between $ZT_{300\ K}$ and $ZT_{1000\ K}$) this difference shows that the most efficient strategy to sample only the top of the distribution depends on *T*. At 300 K the best criterion is to choose two elements with similar values in Pettifor's chemical scale as A and B. Through considerations of electron-phonon scattering, a similar rule—a negative correlation between differences in electronegativity and good bulk thermoelectric properties—has been suggested by several authors.[47,48] Here the situation is different. In nanograined materials the dominant scattering mechanism is, by construction, grain boundary scattering. Thus, only electronic and phononic band structures matter. In this case, an analysis of the percentiles of P/λ and κ/λ of compounds in the best-*ZT* category with respect to the percentiles of the full population shows that the best nanograined thermoelectrics at 300 K outperform the rest mainly because of their lower lattice thermal conductivity. This can be attributed to their larger lattice constants, as explained above. A possible explanation of the connection between $\Delta\chi_{AB}$ and a_0 is that compounds with a low $\Delta\chi_{AB}$ tend to be formed by elements from the regions of the periodic table with the largest atomic radii.

At 1000 K, however, it is advantageous to select out HHs where A's and B's atomic numbers differ by less than 10. Alone, the condition is not sufficient to put the probability of choosing one of the best compounds above 50%. Further splits are then necessary. The optimal route is completed by ensuring that the element acting as X has χ coming from the right-hand half of the periodic table and is smaller than 1.1. The difference in criteria between the two studied temperatures is expected considering the more even mixture of n-type and p-type doped materials at 1000 K, and the increased relevance of electrical transport properties at that temperature. As the contribution of electrons to thermal conduction gets higher, the role of the power factor in determining the best performing compounds increases. In view of these data, the condition $\Delta Z_{AB} < 10$ is clearly connected with low power factors.

To complete the analysis, we also examine the effect of having particular elements either in the {A,B} positions or as X. The most effective elements are those pushing the compound beyond the 75th percentile of the *ZT* distribution. We obtain

the probabilities for positions' types and for temperatures. We select the elements improving the probability above the average (25% by percentile definition). We also impose the constraint that such elements must appear in at least two compounds in the correct position. At 300 K the elements most likely to yield a good thermoelectric HH are {V, Ga, Na, Al, Si, Zr, Sn} as A or B, and Co as X. At 1000 K they are {Na, Al, Si, Ti, Sn} and Co, respectively.

The full list of conditional probabilities is provided in the Supporting Information. The noticeable overlap between the best candidates at both temperatures is another indicator of the correlation between room- and high-temperature behaviors. This is advantageous from an experimental point of view, as it means that some HHs may be tuned to yield good thermoelectric efficiencies at a wide range of temperatures.

Overall, the best five compounds are:

Room-*T*: BiBaK, SbNaSr, AuAlHf, CoBiZr and RhSnTa.

High-*T*: BiBaK, RhSnTa, AuAlHf, CoBiZr, and CoAsHf.

3. Conclusion

We have extracted and examined the 75 thermodynamically stable HH semiconductors out of a library of 79,057 AFLOWLIB HH entries. We have characterized their thermoelectric properties in nanograined form using a completely ab initio approach. The results show that nanograined HHs have significantly higher overall *ZT*s than IV and III–V semiconductors. A large number of potential compounds with $ZT > 0.5$ at room temperature and $ZT > 2$ at high temperatures are competitive with the state of the art. Such high values of *ZT* are caused by average thermal conductivities and very high power factors in the nanograined regime.

The two key properties for high *ZT* are a large lattice parameter and either a wide gap (at high temperatures), or a large effective mass of holes (at room temperature). The presented recursive partitioning algorithm unveils simple recipes to choose, with high probability, a good nanograined thermoelectric half-Heusler in either of the two temperature regimes. These practical selection criteria can stimulate experimental research for improving thermoelectric performance of HH semiconductors.

4. Experimental Section

AFLOWLIB Repository of Half-Heusler Systems: The 79 057 half-Heusler systems are calculated with the high-throughput framework[28,33,36,49] AFLOW based on ab initio calculations of the energies by the VASP software.[50] Projector augmented waves (PAW) pseudopotentials,[51] and Perdew, Burke and Ernzerhof exchange-correlation functionals[52] are used. The AFLOWLIB energies are calculated at zero temperature and pressure, with spin polarization and without zero-point motion or lattice vibrations. All crystal structures are fully relaxed (cell volume, spin, shape, and the basis atom coordinates inside the cell). Initial conditions were ferromagnetic; no antiferromagnetic configurations are tried because of the low magnetic ordering (if any) expected in semiconductors. Numerical convergence to about 1 meV/atom is ensured by a high energy cutoff (30% higher than the highest energy cutoff for the pseudo-potentials of the components), and by the dense 6000 k-points per reciprocal atom Monkhorst-Pack meshes.[53] For each compound within the AFLOWLIB repository we extract the symmetries, band structures, band gaps, and effective masses of electrons and holes. These data can be freely downloaded from the consortium repository AFLOWLIB.org directly or automatically by using the standardized application program interface.[54]

Transport Coefficients: In the nanograined limit we have:

$$\sigma = \lambda \frac{e^2}{k_B T} M_0^{(FD)} \tag{2a}$$

$$S = \lambda \frac{\lambda}{\sigma} \frac{e}{k_B T^2} M_1^{(FD)} \tag{2b}$$

$$\kappa_e = \lambda \frac{1}{k_B T^2} M_2^{(FD)} - \sigma S^2 T \tag{2c}$$

$$\kappa_l = \lambda \frac{1}{k_B T^2} M_2^{(BE)} \tag{2d}$$

Here, k_B is the Boltzmann constant and e the elementary unit of charge, and we define the integrals:

$$M_n^{(FD)} = \sum_\alpha \int_{BZ} f_{FD}\left(f_{FD} - 1\right) \left| v_{a,k}^{(z)} \right| \left(\epsilon_{a,k} - \mu\right)^n \frac{d^3k}{(2\pi)^3} \tag{3a}$$

$$M_n^{(BE)} = \sum_\alpha \int_{BZ} f_{BE}\left(f_{BE} + 1\right) \left| v_{\alpha,q}^{(z)} \right| \left(\hbar\omega_{\alpha,q} - \mu\right)^n \frac{d^3k}{(2\pi)^3} \tag{3b}$$

where f_{FD} (f_{BE}) is the Fermi-Dirac (Bose-Einstein) distribution, the α index runs over electronic (phonon) bands, $v_{a,k}^{(z)}\left(v_{\alpha,q}^{(z)}\right)$ is the electronic (phonon) group velocity in the transport direction and $\epsilon_{a,k} - \mu\left(\hbar\omega_{\alpha,q}\right)$ is the difference between the energy of the corresponding carriers and the chemical potential, which is zero for phonons.

Interatomic Force Constants (IFCs) and Phonon Dispersions: $3 \times 3 \times 3$ supercells are used in second-order IFC calculations. The Phonopy[55] package is used to generate a minimal set of atomic displacements by harnessing the space group of the crystal structure. $3 \times 3 \times 3$ Monkhorst-Pack k-point grids are employed. Spin polarization is excluded to improve speed. Phonon dispersions are obtained as the square roots of the eigenvalues of the dynamical matrix. This matrix is built by combining the Fourier transform of the IFC matrix with a non-analytic correction to account for long-range Coulomb interactions and reproduce LO-TO splitting.[56] The ingredients for the latter are the dielectric tensor of the solid and a set of Born effective charges, obtained using density functional perturbation theory as implemented in VASP. We employ $32 \times 32 \times 32$ Monkhorst-Pack q-point integration grids in the Brillouin zone to approximate the integrals $M_2^{(BE)}$ needed for Equation 2d.

Electronic Transport Properties: To calculate $M_n^{(FD)}$, defined by Equation 3a, we have customized BoltzTraP[57] to work under the constant-mean-free-path ansatz. The patched version of BoltzTraP is available from https://bitbucket.org/sousaw/boltztrap-lambda. BoltzTraP is based on a smoothed Fourier interpolation of the electronic bands. As input, we provide electronic eigenenergies for each system computed on an $80 \times 80 \times 80$ Monkhorst-Pack k-point grid.

Doping: The effect of doping is simulated with rigid displacements of the chemical potential. For each compound and each temperature, we select the doping level optimizing *ZT*. As mentioned before, the carrier concentration is $\leq 10^{21}$ cm^{-3}, within the doping limits typical of experimental HH thermoelectrics.[1] Numerous references have shown this approximation to be applicable in the typical regimes of thermoelectric interest.[36,58–60]

Supporting Information

Supporting Information is available from the Wiley Online Library or from the authors.

Acknowledgements

This work is partially supported by the French "Carnot" project SIEVE, by DOD-ONR (N00014–13–1–0635, N00014–11–1–0136, and N00014–09–1–0921), by DOE (DE-AC02–05CH11231, BES #EDCBEE) and by Duke University – Center for Materials Genomics. The consortium AFLOWLIB.org acknowledges the CRAY corporation for computational assistance.

Received: April 14, 2014
Revised: July 22, 2014
Published online: September 15, 2014

[1] G. J. Snyder, E. S. Toberer, *Nat. Mater.* **2008**, *7*, 105.
[2] S. Curtarolo, G. L. W. Hart, M. Buongiorno Nardelli, N. Mingo, S. Sanvito, O. Levy, *Nat. Mater.* **2013**, *12*, 191.
[3] G. J. Snyder, T. S. Ursell, *Phys. Rev. Lett.* **2003**, *91*, 148301.
[4] C. B. Vining, *Nat. Mater.* **2009**, *8*, 83.
[5] J.-F. Li, W.-S. Liu, L.-D. Zhao, M. Zhou, *NPG Asia Mater.* **2010**, *2*, 152.
[6] B. M. Curtin, E. W. Fang, J. E. Bowers, *J. Electron. Mater.* **2012**, *41*, 887.
[7] Y. Pei, J. Lensch-Falk, E. S. Toberer, D. L. Medlin, G. J. Snyder, *Adv. Func. Mater.* **2011**, *21*, 241.
[8] S. K. Bux, R. G. Blair, P. K. Gogna, H. Lee, G. Chen, M. S. Dresselhaus, R. B. Kaner, J.-P. Fleurial, *Adv. Func. Mater.* **2009**, *19*, 2445.
[9] Y. Lan, B. Poudel, Y. Ma, D. Wang, M. S. Dresselhaus, G. Chen, Z. F. Ren, *Nano Lett.* **2009**, *9*, 1419.
[10] S. J. Poon, A. S. Petersen, D. Wu, *Appl. Phys. Lett.* **2013**, *102*, 173110.
[11] J. R. Sootsman, J. He, V. P. Dravid, C.-P. Li, C. Uher, M. G. Kanatzidis, *J. Appl. Phys.* **2009**, *105*, 083718.
[12] Y. Gelbstein, B. Dado, O. Ben-Yehuda, Y. Sadia, Z. Dashevsky, M. P. Dariel, *Chem. Mater.* **2010**, *22*, 1054.
[13] B. Poudel, Q. Hao, Y. Ma, Y. Lan, A. Minnich, B. Yu, X. Yan, D. Wang, A. Muto, D. Vashaee, X. Chen, J. Liu, M. S. Dresselhaus, G. Chen, Z. Ren, *Science* **2008**, *320*, 634.
[14] K. Biswas, J. He, I. D. Blum, C.-I. Wu, T. P. Hogan, D. N. Seidman, V. P. Dravid, M. G. Kanatzidis, *Nature* **2012**, *489*, 414.
[15] A. I. Hochbaum, R. Chen, R. D. Delgado, W. Liang, E. C. Garnett, M. Najarian, A. Majumdar, P. Yang, *Nature* **2008**, *451*, 163.
[16] G. K. H. Madsen, *J. Am. Chem. Soc.* **2006**, *128*, 12140.
[17] R. V. Chepulskii, S. Curtarolo, *Phys. Rev. B* **2009**, *79*, 134203.
[18] W. Xie, A. Weidenkaff, X. Tang, Q. Zhang, J. S. J. Poon, T. M. Tritt, *Nanomaterials* **2012**, *2*, 379.
[19] X. Yan, G. Joshi, W. Liu, Y. Lan, H. Wang, S. Lee, J. W. Simonson, S. J. Poon, T. M. Tritt, G. Chen, *Nano Lett.* **2011**, *11*, 556.
[20] S. J. Poon, D. Wu, S. Zhu, W. Xie, T. M. Tritt, P. Thomas, R. Venkatasubramanian, *J. Mater. Res.* **2011**, *26*, 2795.
[21] C. Uher, J. Yang, G. P. Meisner, in *Eighteenth International Conference on Thermoelectrics*, IEEE, New York **1999**.
[22] S. R. Culp, J. W. Simonson, S. J. Poon, V. Ponnambalam, J. Edwards, T. M. Tritt, *Appl. Phys. Lett.* **2008**, *93*, 022105.
[23] J. Yang, H. Li, T. Wu, W. Zhang, L. Chen, J. Yang, *Adv. Func. Mater.* **2008**, *18*, 2880.
[24] D. Wee, B. Kozinsky, B. Pavan, M. Fornari, *J. Elec. Mat.* **2012**, *41*, 977.
[25] Y. Matsumoto, H. Koinuma, T. Hasegawa, I. Takeuchi, F. Tsui, Y. K. Yoo, *MRS Bull.* **2003**, *28*, 734.
[26] K. Yang, W. Setyawan, S. Wang, M. Buongiorno Nardelli, S. Curtarolo, *Nat. Mater.* **2012**, *11*, 614.
[27] S. Curtarolo, W. Setyawan, S. Wang, J. Xue, K. Yang, R. H. Taylor, L. J. Nelson, G. L. W. Hart, S. Sanvito, M. Buongiorno Nardelli, N. Mingo, O. Levy, *Comp. Mat. Sci.* **2012**, *58*, 227.
[28] S. Curtarolo, W. Setyawan, G. L. W. Hart, M. Jahnatek, R. V. Chepulskii, R. H. Taylor, S. Wang, J. Xue, K. Yang, O. Levy, M. Mehl, H. T. Stokes, D. O. Demchenko, D. Morgan, *Comp. Mat. Sci.* **2012**, *58*, 218.
[29] G. Bergerhoff, R. Hundt, R. Sievers, I. D. Brown, *J. Chem. Inf. Comput. Sci.* **1983**, *23*, 66.
[30] FIZ Karlsruhe and NIST, Inorganic Crystal Structure Database, http://icsd.fiz-karlsruhe.de/icsd/
[31] W. Bazela, A. Szytula, *Phys. Status Solidi A* **1981**, *66*, 45.
[32] J. Carrete, W. Li, N. Mingo, S. Wang, S. Curtarolo, *Phys. Rev. X* **2014**, *4*, 011019.
[33] W. Setyawan, S. Curtarolo, *Comp. Mat. Sci.* **2010**, *49*, 299.
[34] P. G. Klemens, *Int. J. Thermophys.* **1994**, *15*, 1345.
[35] J. Callaway, *Phys. Rev.* **1959**, *113*, 1046.
[36] S. Wang, Z. Wang, W. Setyawan, N. Mingo, S. Curtarolo, *Phys. Rev. X* **2011**, *1*, 021012.
[37] N. Mingo, D. A. Stewart, D. A. Broido, L. Lindsay, W. Li, in *Length-Scale Dependent Phonon Interactions*, Springer, New York **2014**.
[38] S. Tamura, *Phys. Rev. B* **1983**, *27*, 858.
[39] A. Kundu, N. Mingo, D. A. Broido, D. A. Stewart, *Phys. Rev. B* **2011**, *84*, 125426.
[40] J. M. Ziman, *Electrons and Phonons: The Theory of Transport Phenomena in Solids*, Oxford University Press, New York **2001**.
[41] Z. Wang, J. E. Alaniz, W. Jang, J. E. Garay, C. Dames, *Nano Lett.* **2011**, *11*, 2206.
[42] M. Bachmann, M. Czerner, C. Heiliger, *Phys. Rev. B* **2012**, *86*, 115320.
[43] J. E. Parrott, *J. Phys. Chem.* **1969**, *2*, 147.
[44] L. Pauling, *The Nature of the Chemical Bond and the Structure of Molecules and Crystals: An Introduction to Modern Structural Chemistry*, 3rd ed., Cornell University Press, New York **1960**.
[45] D. G. Pettifor, *Sol. State Commun.* **1984**, *51*, 31.
[46] L. Breiman, J. Friedman, C. J. Stone, R. A. Olshen, *Classification and Regression Trees*, Chapman & Hall, Boca Raton **1984**.
[47] G. A. Slack, in *CRC Handbook of Thermoelectrics* (Ed: D. M. Rowe), CRC Press, Boca Raton **1995**.
[48] G. D. Mahan, in *Solid State Physics*, Vol. *51* (Eds: H. Ehrenreich, F. Spaepen), Academic Press, New York **1997**.
[49] W. Setyawan, R. M. Gaume, S. Lam, R. S. Feigelson, S. Curtarolo, *ACS Comb. Sci.* **2011**, *13*, 382.
[50] G. Kresse, J. Hafner, *Phys. Rev. B* **1993**, *47*, 558.
[51] P. E. Blöchl, *Phys. Rev. B* **1994**, *50*, 17953.
[52] J. P. Perdew, K. Burke, M. Ernzerhof, *Phys. Rev. Lett.* **1996**, *77*, 3865.
[53] H. J. Monkhorst, J. D. Pack, *Phys. Rev. B* **1976**, *13*, 5188.
[54] R. H. Taylor, F. Rose, C. Toher, O. Levy, K. Yang, M. Buongiorno Nardelli, S. Curtarolo, *Comp. Mat. Sci.* **2014**, *93*, 178–192.
[55] A. Togo, F. Oba, I. Tanaka, *Phys. Rev. B* **2008**, *78*, 134106.
[56] Y. Wang, J. J. Wang, W. Y. Wang, Z. G. Mei, S. L. Shang, L. Q. Chen, Z. K. Liu, *J. Phys.: Condens. Matter* **2010**, *22*, 202201.
[57] G. K. Madsen, D. J. Singh, *Computer Phys. Commun.* **2006**, *175*, 67–71.
[58] O. D. Restrepo, K. Varga, S. T. Pantelides, *Appl. Phys. Lett.* **2009**, *94*, 212103.
[59] A. Selloni, S. T. Pantelides, *Phys. Rev. Lett.* **1982**, *49*, 586.
[60] S. Lee, P. von Allmen, *Appl. Phys. Lett.* **2006**, *88*, 022107.